JOURNAL OF QUATERNARY SCIENCE (2021) **36**(2) 169–179 ISSN 0267-8179. DOI: 10.1002/jqs.3265

JQS Journal of Quaternary Science QRA Quaternary Research Association

# A history of violence: magma incubation, timing and tephra distribution of the Los Chocoyos supereruption (Atitlán Caldera, Guatemala)

**ALEJANDRO CISNEROS DE LEÓN,[1]* JULIE C. SCHINDLBECK-BELO,[1,2] STEFFEN KUTTEROLF,[2] MARTIN DANIŠÍK,[3] AXEL K. SCHMITT,[1] ARMIN FREUNDT,[2] WENDY PÉREZ,[2] JANET C. HARVEY,[1] KUO-LUNG WANG[4,5] and HAO-YANG LEE[4]**

[1]Institut für Geowissenschaften, Universität Heidelberg, Im Neuenheimer Feld 234-236, Germany
[2]GEOMAR Helmholtz Centre for Ocean Research Kiel SFB574, Wischhofstraße 1-3, Kiel, 24148, Germany
[3]GeoHistory Facility, John de Laeter Centre, TIGeR, Curtin University, Perth, WA, 6845, Australia
[4]Institute of Earth Sciences, Academia Sinica, Taipei, 11529, Taiwan
[5]Department of Geosciences, National Taiwan University, Taipei, Taiwan

Received 24 January 2020; Revised 10 November 2020; Accepted 29 November 2020

ABSTRACT: The climactic Los Chocoyos (LCY) eruption from Atitlán caldera (Guatemala) is a key chronostratigraphic marker for the Quaternary period given the extensive distribution of its deposits that reached both the Pacific and Atlantic Oceans. Despite LCY tephra being an important marker horizon, a radioisotopic age for this eruption has remained elusive. Using zircon (U–Th)/He geochronology, we present the first radioisotopically determined eruption age for the LCY of 75 ± 2 ka. Additionally, the youngest zircon crystallization $^{238}U$–$^{230}Th$ rim ages in their respective samples constrain eruption age maxima for two other tephra units that erupted from Atitlán caldera, W-Fall (130 $^{+16}/_{-14}$ ka) and I-Fall eruptions (56 $^{+8.2}/_{-7.7}$ ka), which under- and overlie LCY tephra, respectively. Moreover, rim and interior zircon dating and glass chemistry suggest that before eruption silicic magma was stored for >80 kyr, with magma accumulation peaking within *ca.* 35 kyr before the LCY eruption during which the system may have developed into a vertically zoned magma chamber. Based on an updated distribution of LCY pyroclastic deposits, a new conservatively estimated volume of ~1220 ± 150 km$^3$ is obtained (volcanic explosivity index VEI > 8), which confirms the LCY eruption as the first-ever recognized supereruption in Central America.


KEYWORDS: $^{238}U$–$^{230}Th$ disequilibrium; geochronology; tephrochronology; (U–Th)/He; zircon

## Introduction

Caldera-forming supereruptions (volcanic explosivity index VEI 8) are among the most energetic geological events on Earth with well-documented impacts on climate and the biosphere, yet they are only known from the geological record as no such eruption has occurred in historical times (Miller and Wark, 2008; Newhall *et al.*, 2018). The broad airborne and ground-hugging dispersal of volcanic particles, along with the release of substantial climate-forcing gases (e.g. $SO_2$ and oxidized derivatives; Metzner *et al.*, 2014; Krüger *et al.*, 2015; Kutterolf *et al.*, 2015; Brenna *et al.*, 2019, 2020), represent serious hazards from local to global scales (Self, 2006; Miller and Wark, 2008). Improving knowledge of magma storage and eruption chronologies as well as the distribution of pyroclastic materials during caldera-forming eruptions are essential prerequisites to reconstruct past eruptive behaviors and assess future risks. This is especially true for eruptions such as the Los Chocoyos (LCY) event sourced from Atitlán caldera (Guatemala) that has produced atypical long-runout pyroclastic density currents (PDCs) with a particularly destructive power due to the rapid movement of hot mixtures of gas and rock across the ground surface (Koch and Mclean, 1975).

The LCY is the largest Quaternary eruption in the Central American volcanic arc (CAVA; Rose *et al.*, 1987) and it ranks among the largest known individual volcanic events worldwide (>1000 km$^3$; VEI > 8; Kutterolf *et al.*, 2016; Newhall *et al.*, 2018). It has been widely used as a key chronostratigraphic marker for relative dating of paleoenvironmental, paleoclimate and volcanic events throughout Central America and adjacent marine basins in the Pacific Ocean, the Caribbean Sea and the Gulf of Mexico (e.g. IODP and ICDP; Bowles *et al.*, 1973; Hahn *et al.*, 1979; Drexler *et al.*, 1980; Cadet *et al.*, 1982a, 1982b; Ledbetter, 1982, 1985; Pouclet *et al.*, 1985; Rabek *et al.*, 1985; Hodell *et al.*, 2008; Kutterolf *et al.*, 2008a, 2008b, 2015, 2016). The age of this tephra has long been inferred as *ca.* 84 ka BP from $\delta^{18}O$ stratigraphy of marine carbonates (Drexler *et al.*, 1980), but despite its importance to many aspects of Quaternary geosciences and the hazard potential that Atitlán caldera poses itself, the inferred date for the LCY eruption has not been independently tested through radioisotopic methods. Multiple attempts of radioisotopic confirmation of the $\delta^{18}O$ age for LCY have failed due to the inherent limitations of radiocarbon dating (which is practically limited to <50 ka) and a lack of suitable materials for $^{40}Ar/^{39}Ar$ analysis (e.g. Bonis *et al.*, 1966; Kennett and Huddlestun, 1972; Bowles *et al.*, 1973; Koch and Mclean, 1975; Hahn *et al.*, 1979; Drexler *et al.*, 1980; Rose *et al.*, 1999; Brocard and Morán-Ical, 2014). Moreover, little is known about the timescales of magma accumulation underneath Atitlán caldera before and after its supereruption.

Zircon is a chemically and physically resistant mineral that has the potential to accurately record the age of rocks throughout Earth's history. The $^{238}U$–$^{230}Th$ and U–Pb isotopic systems in zircon are largely undisturbed by diffusion even at magmatic

*Correspondence: Alejandro Cisneros de León
Email: cisneros.deleon@outlook.de

temperatures, thus yielding reliable crystallization ages and constraints on the longevity of magmatic systems. By contrast, radiogenic $^{4}$He remains highly mobile in zircon until reaching its low closure temperature (150–220 °C; Reiners *et al.*, 2004; Guenthner *et al.*, 2013). In volcanic rocks, this occurs upon rapid quenching of zircon-bearing magma at the Earth's surface, and hence (U-Th)/He ages are generally interpreted as eruption ages unless disturbed by subsequent heating events (Danišík *et al.*, 2017). For young zircon where the intermediate daughter isotope $^{230}$Th is in disequilibrium, $^{238}$U–$^{230}$Th analysis of individual crystals is an essential prerequisite for accurate (U–Th)/He zircon eruption age determinations (zircon double-dating, ZDD; Danišík *et al.*, 2017) because significant disequilibrium corrections are required (Farley *et al.*, 2002). Another important constraint from zircon $^{238}$U–$^{230}$Th crystallization dating is that the youngest crystals can provide an upper limit for the eruption age (Schmitt, 2011).

Here, we combine results from fieldwork (mapping) with geochronology using the ZDD method combining U-series and (U–Th)/He ages. This investigation has resulted in the first radioisotopic age determination for the LCY eruption and in a maximum depositional age for the previously undated younger I-Fall eruption. Zircon crystallization ages from LCY and bracketing units also constrain the timescales of magma accumulation before and after the LCY eruption. Based on the new mapping and tephra correlation, we also updated the distribution of PDC deposits from LCY and re-evaluate its eruptive volume applying a geographical information system (GIS) approach. Our results confirm LCY as the first documented Central American VEI 8 supereruption (e.g. Kutterolf *et al.*, 2016).

## Geological background

Atitlán caldera (18 × 12 km, ~600 m depth), located in southwestern Guatemala, results from the youngest of at least three overlapping caldera-forming events that occurred over the last *ca.* 14 million years (Atitlán I: *ca.* 14–11 Ma, Atitlán II: *ca.* 10–8 Ma, Atitlán III: *ca.* 1–0 Ma; Newhall, 1987). During the last caldera-forming phase (Atitlán I) modern Atitlán Lake was created (~300 km$^2$; Fig. 1a). This phase comprised at least three large-scale explosive rhyolitic eruptions including W-Fall eruption at *ca.* 158 ± 3 ka ($^{40}$Ar/$^{39}$Ar; Rose *et al.*, 1999), the colossal LCY eruption estimated at *ca.* 84 ± 5 ka (Drexler *et al.*, 1980) and the I-Fall eruption suite, with a stratigraphically estimated age of >40 ka (Rose *et al.*, 1987). During the estimated 20–27-day duration of the LCY climactic ultra-Plinian eruption (Ledbetter and Sparks, 1979), a >40-km-high eruptive column produced fall-out deposits up to 3.6 m thick in proximal locations, and distal cm-thick deposits spanning from the coast of Texas to the Panama Basin (Fig. 1b; Drexler *et al.*, 1980; Rose *et al.*, 1987; Kutterolf *et al.*, 2016; Schindlbeck *et al.*, 2018). Concurrently, repeated gravitational collapse from the eruptive column produced voluminous PDCs that surmounted remarkably high topographic barriers in the

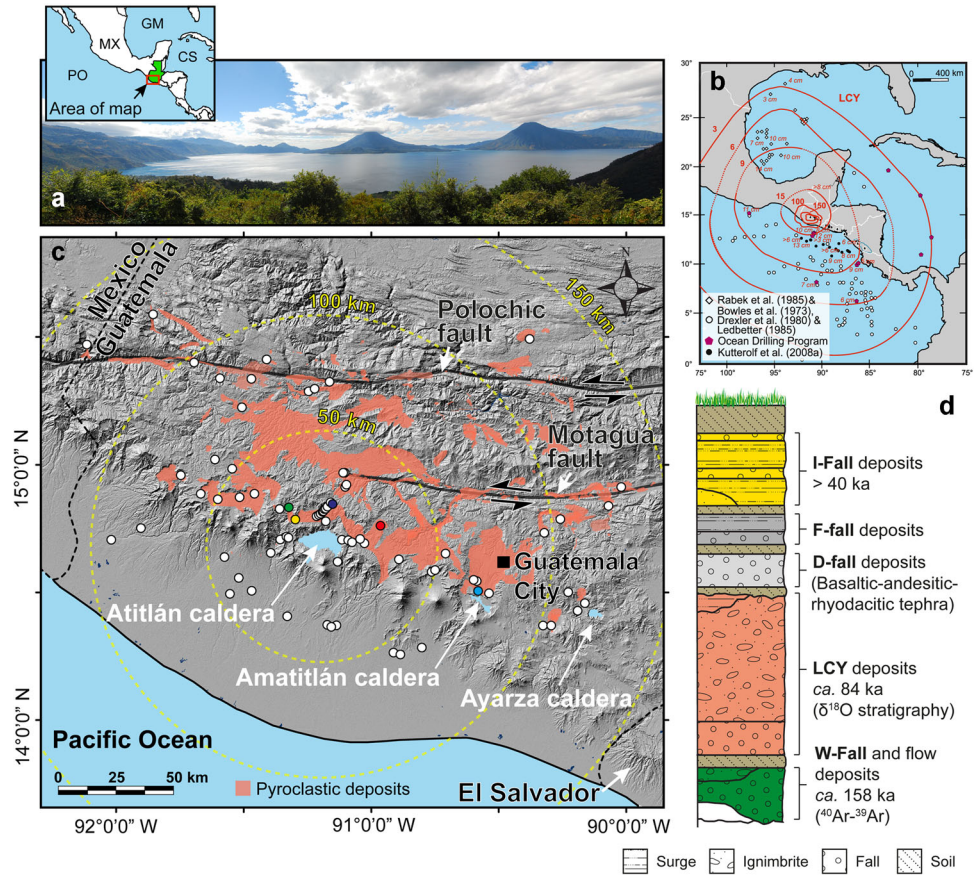


**Figure 1.** (a) Location of Atitlán caldera and overview of Lake Atitlán. (b) Isopach map for LCY fall-out tephra modified from Kutterolf *et al.* (2016). Bold numbers represent isopach thicknesses and numbers in italics give thicknesses at the distal outcrops. Isopachs are taken from Kutterolf *et al.* (2016) and references therein; distal isopachs are constrained by few available data and documented with dotted lines where interpolation between outcrop thickness is weak or missing. Symbols in the map represent the literature sources for the thickness data as given in the legend. (c) Map showing the distribution of exposed ignimbrite (pyroclastic density current, PDC) deposits from the Los Chocoyos eruption. White circles are sampling locations, whereas colored circles are locations of samples used for zircon $^{238}$U–$^{230}$Th crystallization and (U–Th)/He eruption geochronology. Modified from Hahn *et al.* (1979) and Brocard and Morán-Ical (2014). PO = Pacific Ocean; GM = Gulf of Mexico; CS = Caribbean Sea; MX = Mexico. Shaded relief topography based on ASTER GDEM Version 3 (NASA/METI/AIST/Japan Space Systems, and U.S./Japan ASTER Science Team, 2019). (d) Schematic stratigraphic column synthesized from different outcrops of Atitlán deposits with a differentiated stratigraphy of the LCY eruptive sequence modified after Rose *et al.* (1987). [Color figure can be viewed at wileyonlinelibrary.com]

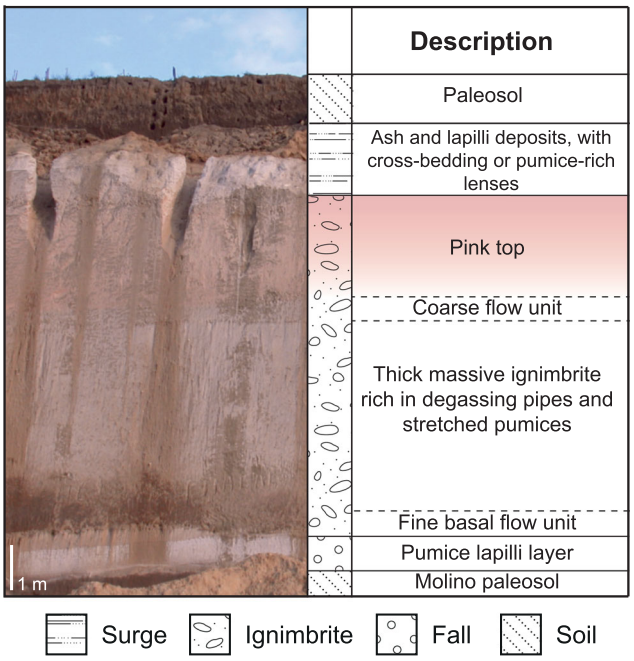


**Figure 2.** Outcrop photograph showing a typical eruptive deposit sequence of the LCY eruption. [Color figure can be viewed at wileyonlinelibrary.com]

Guatemalan highlands with more than ~400-m elevation difference (Koch and Mclean, 1975). These PDCs continued to flow for distances >130 km from the source, filling major drainage basins with up to ~200-m-thick deposits of non-welded pyroclastic particles (Fig. 1c; Koch and Mclean, 1975; Hahn *et al.*, 1979). The LCY eruptive sequence comprises a basal tephra fall-out member (Figs 1d and 2), the largest known in Central America, which is overlain and sometimes partly eroded by a thick (4–200 m) unwelded ignimbrite deposit (characterized by salmon pink top; Fig. 2), and ~1 $km^3$ of surge deposits, which formed during late-stage phreatomagmatic explosions (Rose *et al.*, 1987). Based on distal outcrops at Lake Petén Itzá and offshore data from the Pacific Ocean and the Caribbean Sea, current estimates on mass and tephra volume for the LCY eruption are ~$1.3 \times 10^{15}$ kg and ~1100 $km^3$ (510 $km^3$, dense rock equivalent, DRE), respectively (Kutterolf *et al.*, 2016; Schindlbeck *et al.*, 2018). The older W-Fall and younger I-Fall yield erupted tephra volumes of ~83 $km^3$ (DRE) and ~7 $km^3$ (DRE), respectively (Rose *et al.*, 1987; Kutterolf *et al.*, 2016).

## Methods

Based on established stratigraphy, textural characteristics (Koch and Mclean, 1975) and new mapping of 113 outcrops, 57 potential LCY tephra samples were collected from proximal, medial and distal sites and variable stratigraphic positions (Fig. 1c). Sampling was geographically widespread (mostly radially to the north, west and east of the caldera) and covered stratigraphically distinct levels, which include depositional sub-units, including fall-out, ignimbrite and surge deposits (Fig. 2). Proximal LCY fall-out (G17-26; ~17 km NNE) and ignimbrite (G17-23; ~25 km NE) as well as a medial fall-out (G17-4; ~50 km SE) samples were selected for geochronological analysis on zircon unpolished rims and polished interiors (G17-23) by $^{238}U$–$^{230}Th$ disequilibrium dating using a CAMECA IMS 1280-HR secondary ion mass spectrometer at Heidelberg University, Germany (providing crystallization ages of the outermost crystal face for all samples; Supporting Information Table S1). Additionally, two large silicic eruptions that bracket the LCY eruption (W- and I-Fall) were also sampled for analysis of zircon rim crystallization ages (Table S1). For eruption source identification and correlation purposes, glass shards were analyzed for major and trace element abundances in selected samples from LCY, W- and I-Fall (sub)units. Major element geochemical analyses from glass shards were carried out using electron probe microanalyses at GEOMAR, Kiel, Germany (EMPA; Table S2), whereas trace element concentrations were determined via laser ablation inductively coupled plasma mass spectrometry at the Academia Sinica in Taipei, Taiwan (LA-ICP-MS; Table S2). The (U–Th)/He part of ZDD was conducted at the John de Laeter Centre (Curtin University), Perth, Australia, following protocols described in Danišík *et al.* (2017). The accuracy of the zircon (U–Th)/He dating procedure was monitored by replicate analyses of Fish Canyon Tuff zircon ($n = 12$) measured throughout this study as an internal standard, yielding a mean (U–Th)/He age of $28.4 \pm 0.9$ Ma ($n = 12$; $1\sigma$ uncertainties stated throughout this study; Table S3), which is in good agreement with the reference (U–Th)/He age of $28.3 \pm 1.3$ Ma (Reiners, 2005) and a U-Pb age of $28.48 \pm 0.03$ Ma (Schmitz and Bowring, 2001). To avoid overestimation of the disequilibrium correction, zircon (U–Th)/He ages were corrected following the method of Friedrichs *et al.* (2021) that accounts for intragrain variations in $^{238}U$–$^{230}Th$ disequilibria resulting from protracted crystallization where interiors can be significantly older than rims. The eruption age for single samples was calculated as the error-weighted mean from the disequilibrium-corrected single-grain (U–Th)/He ages and standard errors using IsoplotR (Vermeesch, 2018; Table S3). The final LCY eruption age was calculated from combining the disequilibrium-corrected single-grain (U–Th)/He ages of the three analyzed LCY samples ($n = 48$ grains). Mean square weighted deviation (MSWD) values were >1 in all samples, suggesting non-analytical scatter (e.g. due to heterogeneity in U abundances); to provide a conservative age uncertainty, all standard errors of the weighted average were multiplied by the square root of the MSWD.

### *LCY volume calculation*

The LCY PDC volume was reassessed using GIS-based analysis. The ignimbrite deposit limits (Fig. 3a) were estimated based on the elevation and morphology interpolated from the nearest outcrops and respective thicknesses as well as from interpolated thickness decay to the distance evident by the debris fans visible on Google Earth. The LCY ignimbrite volumes are based on field measurements (Fig. 3a–c; Supporting Information Table S4) plus drill core data from the Quetzaltenango basin of Rose *et al.* (1979). Working in the Universal Transverse Mercator (UTM) coordinate system, ignimbrite volumes were calculated by two methods: (i) from the ignimbrite distribution map (Fig. 3a) in raster format with a 30-m pixel size, by summation of the areas times estimated average thickness; or (ii) from the volume under continuous thickness surfaces interpolated from minimum thickness field observations (Fig. 3b,c). Specific thickness data for LCY are available for 60 locations supplemented by five thickness estimates and interpretation from Rose *et al.* (1979; Fig. 3a; Table S4). The 65 locations provide only minimum deposit thickness estimates, and thus volume calculations are likely to conservatively underestimate the original total volume. Based on the permissible flow directions from Brocard and Morán-Ical (2014), interpolation across the Guatemala highlands proximal to Atitlán is allowed, and no attempt is made to differentiate between thickness variations produced by chan-

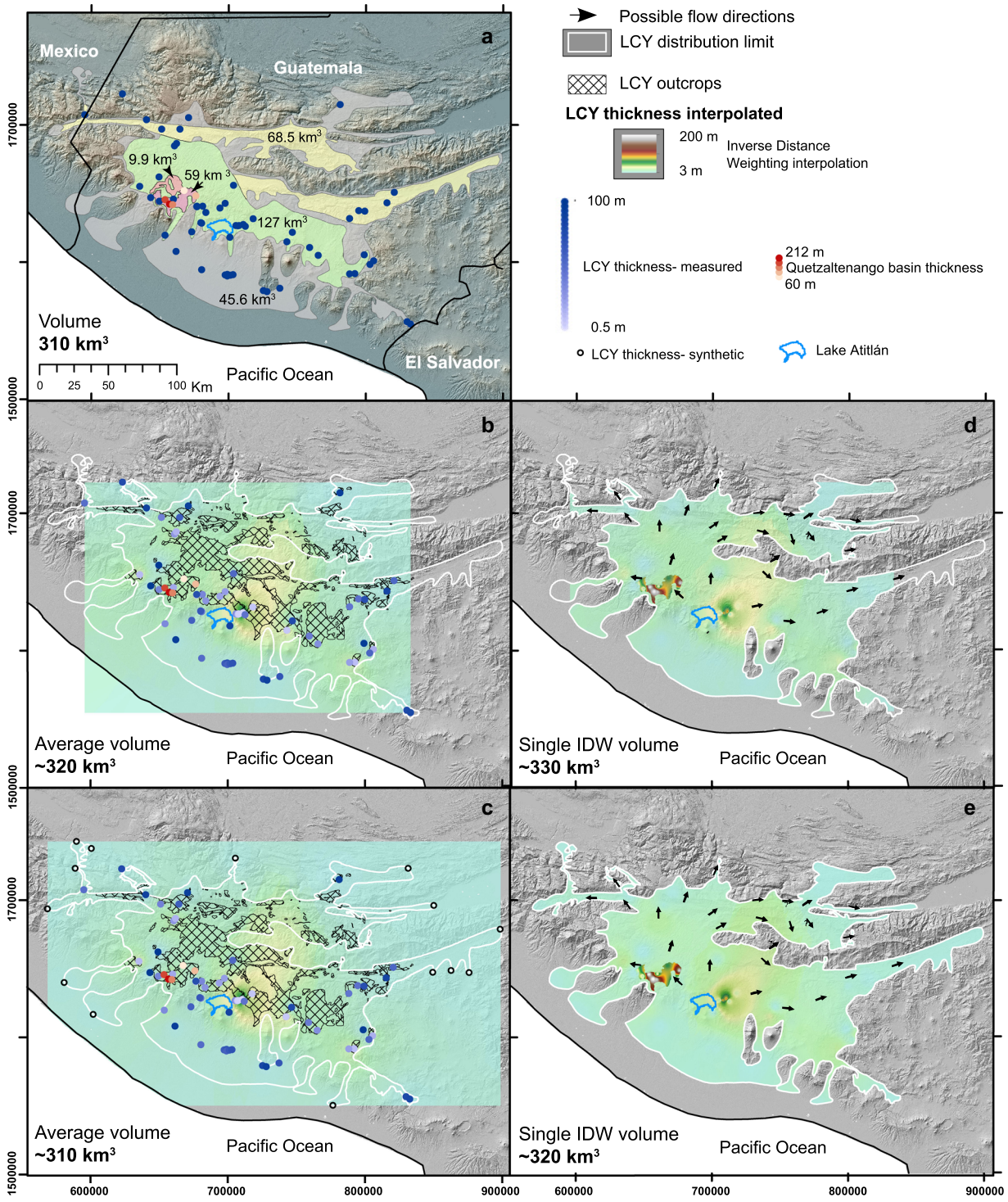


**Figure 3.** Estimate of LCY original ignimbrite distribution based on outcrop thicknesses and interpolated extensions. (a) Colored fields: integrated LCY thickness estimates from measured points and geomorphology of sedimentary basins. Volume estimation computed directly as thickness times area; blue circles represent LCY field thickness measurements. (b,d) LCY potential extent from panel (a) (white outlines); colors represent interpolated thickness using an inverse distance weighting (IDW) algorithm and black hatch areas are combined outcrops from this work and Hahn *et al.* (1979) and Brocard and Morán-Ical (2014); volume estimate from the average of eight different interpolation algorithms. (c,e) Intersection of interpolation hull and estimated 4 m PDC extent; black arrows show possible LCY flow directions from Brocard and Morán-Ical (2014) and volume estimate is from a single IDW algorithm. (b,c) Volume calculation based on interpolation restricted to available field thickness data; interpolation hull limited by measured thickness locations. (d,e) Volume calculations using a 4 m estimated extent of LCY ignimbrite via measured thicknesses and synthetic or extrapolated points. (c,d) Thickness surface for Quetzaltenango basin interpolated separately or with interpolation boundaries depending on the interpolation algorithm. [Color figure can be viewed at wileyonlinelibrary.com]

nelized flow versus 360-degree flooding of the original topography. Data are not evenly distributed among mapped exposures; distal deposits to the north-east are poorly represented, and undocumented. Probably continuous runout deposits down the coastal plain to the south are not encompassed by this volume estimate. As a result, simple interpolated thickness calculations based on the known minimum thicknesses are dependent on the interpolation algorithm. Using ESRI ArcGIS, at a scale of 90 m in UTM, utilizing eight different interpolation algorithms with standard interpolation parameters, interpreted thickness surfaces based on the 65 thickness observations yield a convex hull extent

encompassing the thickness observations, but not the complete perimeter of estimated outcrop extents in Fig. 3(b). To force an extrapolation to the estimated 4-m thickness limit, synthetic points were added to the 4-m perimeter line for a comparison set of volume calculations. Based on Rose *et al.* (1979), interpolation limits were introduced at the boundaries of the Quetzaltenango basin, either through algorithmically derived interpolation barriers or masking. For interpolation algorithms that do not allow an internal interpolation barrier, two interpolation surfaces were derived, the first an interpolation surface derived without the drill core data, and the second with the addition of the drill core data. The interpolated thicknesses within the Quetzaltenango basin from the second interpolation were masked into the first to capture the irregular thickness derived from the flooding of pre-existing basins.

## Results

### *Stratigraphic and textural characteristics of LCY deposits*

The profiles of proximal, medial and distal LCY deposits were investigated and three sub-units were distinguished comprising fall-out, ignimbrite and surge members (Fig. 2). The fall-out member has a basal thin fine ash layer, a middle coarse-ash portion and a thick upper part composed of mostly pumice lapilli supported by a coarse ash matrix. The ignimbrite member comprises a thin layer of coarse ash at the bottom followed by a lithic-rich layer, probably related to the caldera collapse event. The main body of the ignimbrite member is dominated by one or more massive and thick flow units separated by co-ignimbrite lag breccia horizons. Degassing pipes, charcoal and the pink discoloration in the top parts of these deposits are evidence of relatively hot emplacement, yet no welding occurred. Surge deposits at the top of the LCY sequence consist of finely undulated stratified ash deposits. Evidence of wet deposition for surges is provided by accretionary lapilli and flame-like load structures. Surge deposits lack the pink discoloration of the underlying ignimbrite deposits, and degassing pipes are confined to the ignimbrite layers, suggesting a short time-lapse between ignimbrite and surge emplacement as no soil horizon was developed. Moreover, lapilli fall-out layers between ignimbrite and surge deposits west of the caldera may indicate high eruption columns associated with the late phase of the eruption.

### *Glass chemistry*

Major and trace element glass compositional data for newly sampled fall-out and ignimbrite deposits (Fig. 4) agree closely with previously established LCY compositional fields on bivariate diagrams (Kutterolf *et al.*, 2008b, 2016). In contrast, ash particles and pumice clasts from late-stage LCY surges (and in few cases from the ignimbrites) show bimodal and sometimes less evolved ('exotic'; gray circles and squares in Fig. 4a) glass compositions (sometimes within individual pumice clasts) that plot distinctly from known LCY compositional fields. The splitting of glass compositions into high-K and low-K clusters (difference ~2 wt% $K_2O$) reflects the change from high-K biotite-bearing rhyolite in the LCY fall-out to low-K hornblende rhyodacite in the flow deposits that Rose *et al.* (1987) observed in bulk-rock compositions. Major element compositions from W- and I-Fall glasses strongly overlap with LCY compositional fields and older tephras from Atitlán caldera (>158 ka; Kutterolf *et al.*, 2008a, 2016), but many trace element ratios are distinct (e.g., Zr/Nb vs. Ba/La; Fig. 4b). Glass chemical analyses along the LCY eruptive sequence suggest variations towards more heterogeneous melt compositions (Fig. 5) that may be related to the previously described overturn of the magma chamber (Rose *et al.*, 1979).

### *(U–Th)/He and U–Th zircon (ZDD) geochronology*

Disequilibrium-corrected (U–Th)/He analyses of LCY zircon crystals from the proximal fall-out sample (G17-26) average 75 ± 3 ka (MSWD = 4.1; $n$ = 16; Fig. 6a), whereas medial fall-out sample (G17-4) average 76 ± 3 ka (MSWD = 2.5; $n$ = 16; Fig. 6b). Zircon from the proximal ignimbrite deposit (G17-23) yielded an average age of 73 ± 4 ka (MSWD = 3.7; $n$ = 16;

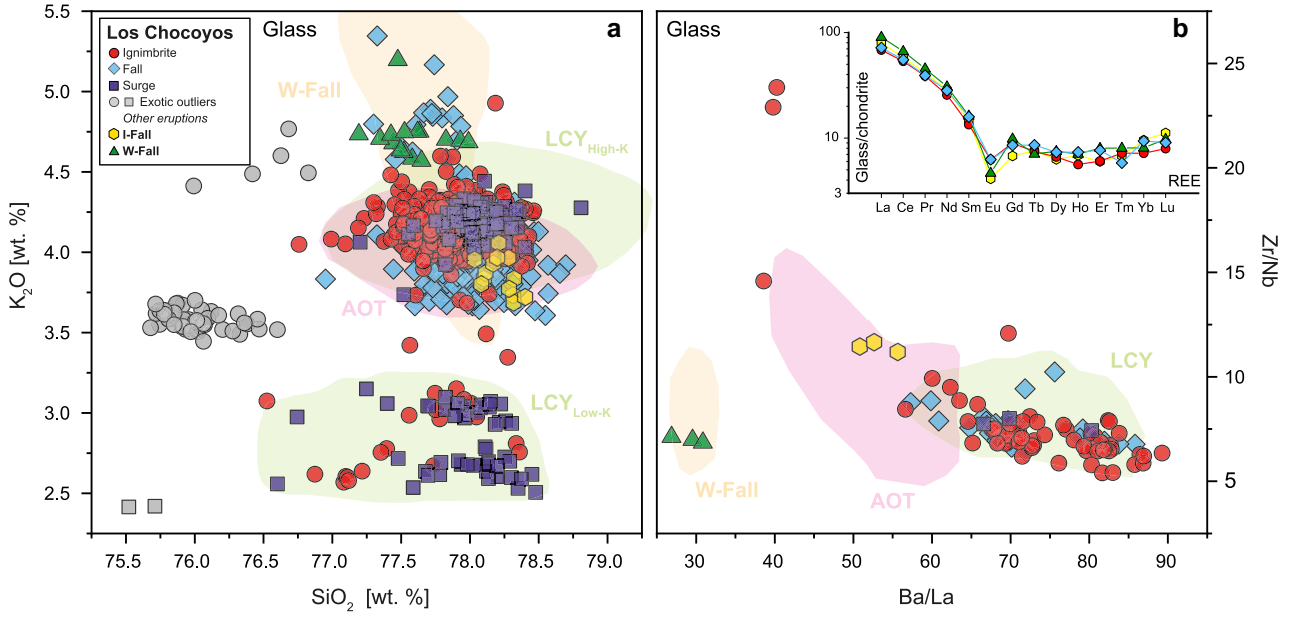


**Figure 4.** Glass major and trace element geochemistry of Atitlán eruptions. (a) $K_2O$ vs $SiO_2$ glass shard compositions of LCY eruptive sequence and W- and I-Fall tephra. (b) Trace element glass shard compositional ratios. Colored fields are based on data for proximal glass compositions from Kutterolf *et al.* (2016) and Schindlbeck *et al.* (2018); the inset shows chondrite-normalized rare earth element patterns for glass compositions. Symbols are single glass shard analysis. Exotic outliers are individual glass shards differing from the bulk of their respective matrix ash or pumice clasts; the origin of the outlier compositions will be investigated elsewhere. AOT = Atitlán older tephra; LCY = Los Chocoyos. [Color figure can be viewed at wileyonlinelibrary.com]

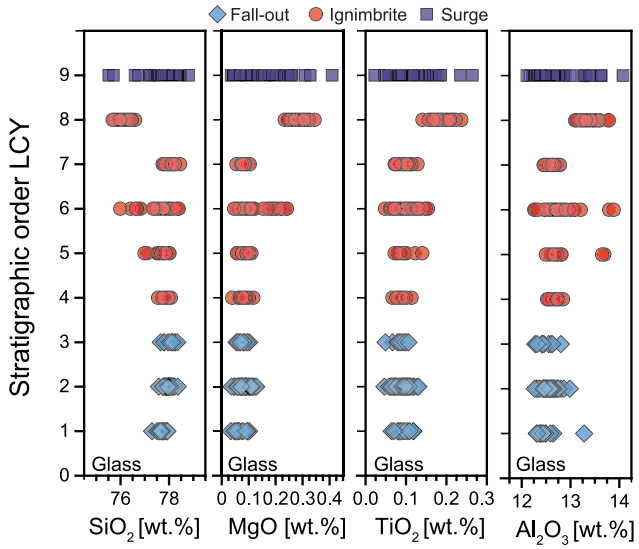


**Figure 5.** Glass compositional variations of LCY tephra in stratigraphic order (not scaled to thickness or volume). Each sub-unit was sampled at a similar stratigraphic level at different locations. [Color figure can be viewed at wileyonlinelibrary.com]

Fig. 6c). Considering all zircon analyses as one population, the weighted mean age and best estimate for the LCY eruption age is 75 ± 2 ka (MSWD = 3.3; $n = 48$; Fig. 6d). This age is proposed as presently the most precise estimate for the age of the LCY eruption.

Zircon U–Th crystallization rim ages for the youngest unit of Atitlán caldera (I-Fall; G17-38) yielded ages ranging from 56 $^{+8}/_{-8}$ to 148 $^{+49}/_{-34}$ ka (Fig. 7a; $n = 29$), with a zircon crystallization age peak in a probability density function (PDF) at *ca.* 75 ka. Proximal (G17-26; $n = 25$) and medial (G17-4; $n = 27$) LCY fall-out samples contain zircon crystals with rim ages ranging from 74 $^{+7}/_{-7}$ to 139 $^{+20}/_{-17}$ ka and 82 $^{+10}/_{-9}$ to 160 $^{+28}/_{-22}$ ka, respectively (Fig. 7b,c); PDFs display zircon crystallization age peaks for the proximal fall-out at *ca.* 87 ka and for the medial fall-out at *ca.* 97 ka. Zircon rims from the LCY ignimbrite (G17-23; $n = 54$) range in age from 80 $^{+14}/_{-12}$ to 197 $^{+62}/_{-39}$ ka (Fig. 7d), whereas zircon interior analyses ($n = 39$) for the same sample show a similar age range and distribution, ranging from 81 $^{+12}/_{-11}$ to 234 $^{+104}/_{-52}$ ka (Fig. 7e) with a few zircon crystals being in secular equilibrium (ages >350 ka, unresolvable by $^{238}$U–$^{230}$Th disequilibrium dating methods). Zircon rim crystallization ages for LCY ignimbrite peak at *ca.* 100 ka, whereas zircon interiors show a slightly older crystallization age peak at *ca.* 110 ka. Multiple spot analyses on sectioned zircon crystals (G17-23) reveal frequent antecrystic domains (derived from earlier crystal mush or solidified portion of the magma chamber; Fig. 8a), whereas domains in secular equilibrium (>350 ka) may be of xenocrystic origin (derived from country-rock). Both are usually partly resorbed and overgrown by juvenile zircon with oscillatory zonation. Ages for antecrystic interiors and their juvenile overgrowths are in most cases indistinguishable within error, despite showing contrasting cathodoluminescence domains and resorption surfaces in between (Fig. 8a). The older W-Fall eruption (G17-42; $n = 23$) yielded zircon rim crystallization ages that range from 130 $^{+16}/_{-14}$ to 303 $^{+\infty}/_{-117}$ ka (Fig. 7f), with a unimodal crystallization age distribution peak at *ca.* 182 ka.

Although similar in age, zircon rims and interiors show a significant difference in ($^{238}$U)/($^{232}$Th) and ($^{230}$Th)/($^{232}$Th) activity ratios. Zircon interiors typically have lower ($^{238}$U)/($^{232}$Th) compared to rims, although some overlap exists (Fig. 9).

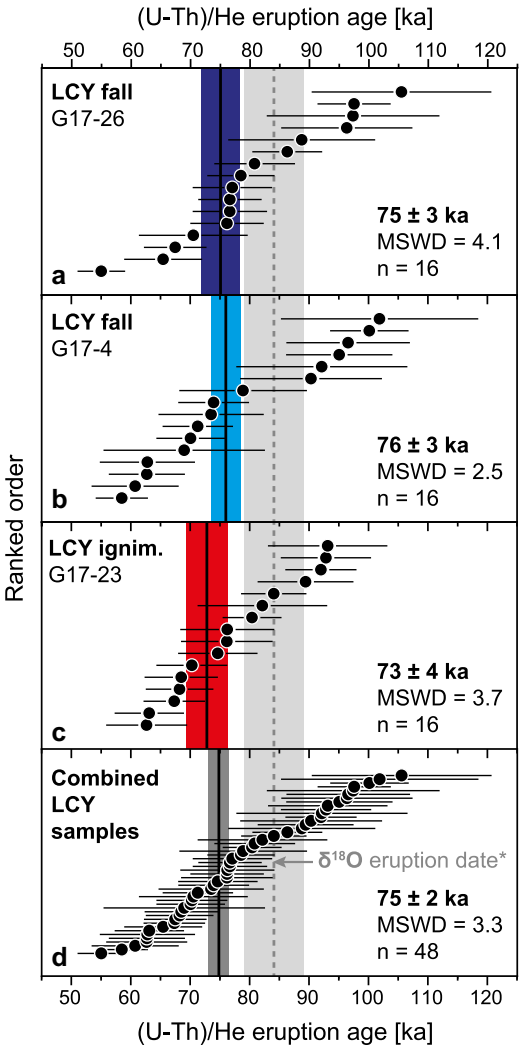


**Figure 6.** (a–c) Disequilibrium-corrected zircon (U–Th)/He eruption dating for LCY units including fall and ignimbrite deposits. Vertical black lines represent weighted average mean eruption age, whereas the dotted gray line indicates published oxygen isotope stratigraphic eruption date of 84 ± 5 ka from Drexler *et al.* (1980). (d) Weighted average mean from combining zircon (U–Th)/He data from all LCY dated samples. Uncertainties are 1σ. [Color figure can be viewed at wileyonlinelibrary.com]

The variability in ($^{238}$U)/($^{232}$Th) might be due to the presence of monazite (Fig. 8b), which occurs relatively frequently in heavy mineral separates from all studied Atitlán caldera eruptions, and which may strongly fractionate Th from U when the melt reaches monazite saturation. Uranium abundances in zircon rims and interiors from ignimbrite sample (G17-23) range from 88 to 834 p.p.m. (average = 316) and from 118 to 4390 p.p.m. (average = 684), respectively. We observe no systematic difference in U concentrations between rims and interiors.

## Discussion

### *Age of the Los Chocoyos supereruption and magma storage timescales*

The zircon (U–Th)/He eruption age for LCY of 75 ± 2 ka is significantly younger than the commonly cited O-isotope stratigraphic age of 84 ± 5 ka (Drexler *et al.*, 1980) and similar within error to the corresponding youngest $^{238}$U–$^{230}$Th zircon ages which date magmatic crystallization (Fig. 7b–e; Table 1). Concordance between (U–Th)/He eruption ages and the

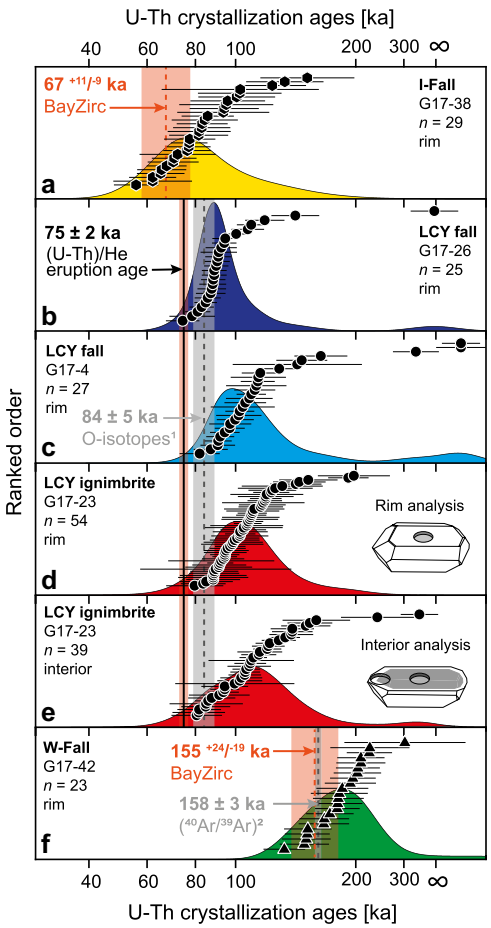


**Figure 7.** Ranked order and relative probability plots of Atitlán caldera zircon crystallization ages. (a) $^{238}U$–$^{230}Th$ zircon rim crystallization ages for the I-Fall unit. (b–e) $^{238}U$–$^{230}Th$ zircon rim and interior crystallization ages for LCY fall and ignimbrite samples. (f) $^{238}U$–$^{230}Th$ zircon rim crystallization ages for the W-Fall unit. The solid black line represents (U–Th)/He-weighted average mean eruption age. Vertical orange dashed lines represent Bayesian eruption estimates following the approach of Keller *et al.* (2018), whereas the dotted gray line represents the O-isotope stratigraphic LCY date from [1]Drexler *et al.*, 1980 and the $^{40}Ar/^{39}Ar$ eruption age from [2]Rose *et al.* (1999). All error bars are 1σ. [Color figure can be viewed at wileyonlinelibrary.com]

youngest $^{238}U$–$^{230}Th$ zircon crystallization ages for each sample provides a first-order consistency check for the ZDD method (e.g. Danišík *et al.*, 2017). Moreover, zircon crystallization ages overlapping with the eruption age suggest that crystallization in this magmatic system was ongoing shortly before eruption. By analogy, we interpret the youngest $^{238}U$–$^{230}Th$ zircon crystallization ages as a proxy for the eruption of W- and I-Fall from Atitlán caldera, although it always should be cautioned that zircon crystallization ages are maximum ages for the eruption. A critical assumption for this is that no zircon dissolution occurred before the eruption, which is supported by the euhedral morphology of the zircon crystals (inset Fig. 9). Hence, the youngest zircon from W-Fall ($130\ ^{+16}/_{-14}$ ka; 1σ) is younger than the existing $^{40}Ar/^{39}Ar$ eruption age of 158 ± 3 ka obtained from low-K plagioclase, although both ages overlap within 95% confidence (Fig. 7f; Rose *et al.*, 1999). There is, however, one younger $^{40}Ar/^{39}Ar$ plagioclase age of 141 ± 3 ka (1σ) reported for W-Fall (Rose *et al.*, 1999). The presence of unsupported $^{40}Ar$ in low-K plagioclase from all Atitlán caldera eruptions has been previously suspected (Rose *et al.*, 1999), and is also evident from I-Fall tephra samples, which yielded apparent $^{40}Ar/^{39}Ar$ ages of 137 ± 3 and 173 ± 16 ka (Rose *et al.*, 1999), despite I-Fall stratigraphically overlying LCY (Fig. 1d). Zircon rim analysis from I-Fall tephra instead yielded crystallization ages as young as $56\ ^{+8.2}/_{-7.7}$ ka, in agreement with stratigraphic relationships. Conservative estimates for the eruption ages for I-Fall and W-Fall based on $^{238}U$–$^{230}Th$ zircon age spectra and Bayesian statistics (Keller *et al.*, 2018) suggest slightly older eruption dates relative to the youngest zircon age in each sample. For the I-Fall zircon spectrum, the Bayesian estimate is $67\ ^{+11}/_{-9}$ ka, whereas for W-Fall it is $155\ ^{+24}/_{-19}$ ka. Applying the same statistical methodology to the eruption-dated LCY zircon samples, Bayesian age estimates are between *ca.* 5 and 15 kyr older than the (U–Th)/He eruption age (Table 1). It is therefore suggested that the youngest-zircon approach is probably a better approximation to eruption ages for I- and W-Falls from zircon crystallization ages.

Protracted zircon crystallization observed in all Atitlán tephras also suggests prolonged evolved magma presence between eruptions (Fig. 7). Zircon crystallization in the Atitlán magmatic system was probably quasi-continuous, acknowledging that $^{238}U$–$^{230}Th$ geochronology alone cannot distinguish between truly continuous crystallization and brief intermittent hiatuses that are below the dating resolution (e.g. Kent and Cooper, 2018). Although recycling of older zircon crystals into subsequent eruptions occurred frequently, as suggested by age zonation documented by multiple dating spots on crystal interiors (Fig. 8), the shifting of the crystallization modes from the age spectra of the different units is also indicative of a progressive younging of the overall zircon population in the system. Zircon age peaks often coincide with major eruptions, possibly as the result of cooling and crystallization of the unerupted magma after a major recharge event (e.g. Klemetti *et al.*, 2011; Klemetti and Clynne, 2014).

Under the assumption that zircon crystallization is a proxy for silicic melt presence in magma chambers, the pre-eruptive residence for silicic magma systems is usually inferred from the difference between zircon crystallization and eruption ages, or the extent of zircon age distributions. The longevity of such systems as inferred from zircon ages is generally in the order of tens to hundreds of thousands of years (e.g. Bacon and Lowenstern, 2005; Bachmann *et al.*, 2007; Simon *et al.*, 2008). A correlation between long repose periods with eruption magnitude has been suggested for some multi-cycle calderas (e.g. Yellowstone, western USA, and Toba, Indonesia; Reid, 2008; Simon *et al.*, 2008), although recent studies have shown that large eruptions can also be assembled within a few tens of thousands of years or even less (e.g. Wotzlaw *et al.*, 2014; Rivera *et al.*, 2016). The zircon ages from LCY suggest a quasi-continuous history of silicic magma accumulation in the shallow crust over at least >80 kyr before its supereruption (Table 1). Despite the large difference in erupted volumes of LCY with older W-Fall and I-Fall eruptions, the magma storage timescales are of the same order of magnitude (*ca.* 60–80 kyr), discarding a correlation of magma longevity with eruption magnitude.

Partial overlap in LCY zircon ages with those of the preceding W-Fall eruption may suggest that unerupted W-Fall magma contributed material to the subsequent LCY magma chamber. Similarly, the younger I-Fall eruption appears to have partially tapped magma leftovers from the LCY eruption given the significant overlap of zircon ages between both eruptions (Fig. 7). Although more geochemical data are needed to trace magma inheritance from one to another eruption, overlapping glass major and trace element data (Fig. 4; Supporting Information Fig. S1) suggest a probable genetical relationship, with some compositional differences that can be explained by mixing between distinct magma reservoirs and crystal fractionation processes.

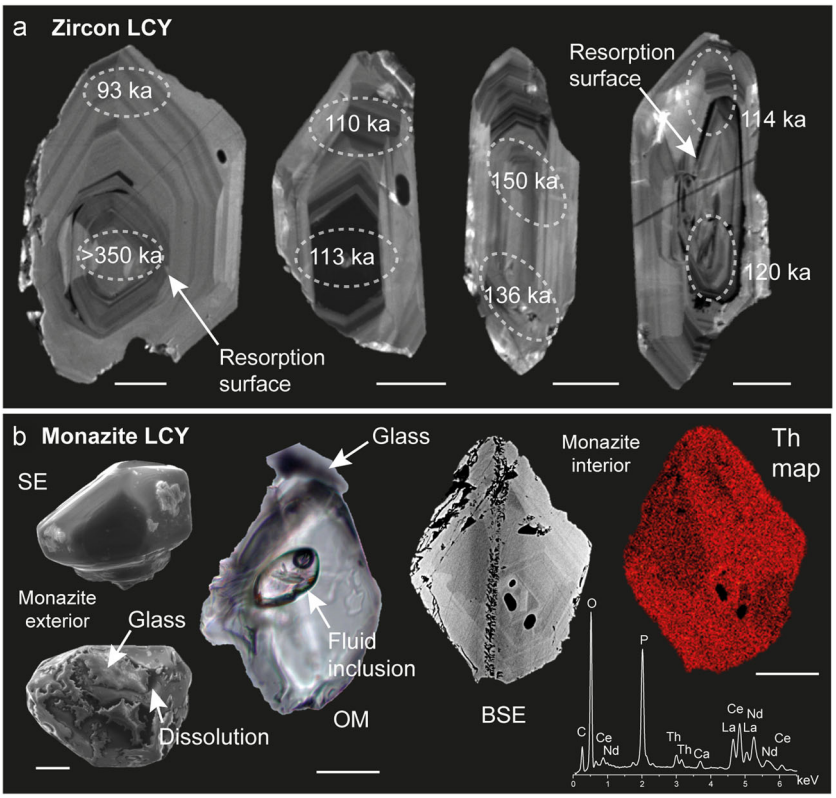


**Figure 8** (a) Cathodoluminescence images of selected LCY ignimbrite zircon crystal interiors with respective $^{238}U$–$^{230}Th$ crystallization ages. White dashed ellipses represent the location and size of the ion beam analysis spot. (b) External and internal morphologies of monazite crystals that are typically found in LCY deposits. SE = secondary electrons; OM = optical microscope; BSE = back-scattered electrons. Scale bar represents in all cases 20 µm. [Color figure can be viewed at wileyonlinelibrary.com]

Although the proportion of inherited W-Fall magma in the growing LCY chamber is difficult to determine, the dominant zircon crystallization age peaks between *ca.* 87 and 110 ka recorded by zircon rims and interiors suggest extensive zircon nucleation and crystallization at a time that significantly post-dates the W-Fall event. Partially resorbed antecrysts overgrown by juvenile domains with indistinguishable ages of *ca.* 100 ka (Fig. 8) indicate that zircon saturation was re-established rapidly following magma recharge, where transient heating coupled with chemical changes towards less evolved compositions may have caused partial resorption of pre-existing zircon. Although a magma build-up time of <35 kyr can be inferred from the difference between the LCY eruption age and the zircon crystallization age peaks of LCY samples, it would be premature to postulate continuous magma residence for the LCY reservoir. The reason to be cautious in inferring continuous magma residence is because prismatic zircon faces, which record the last crystallization event of an individual zircon crystal, cover nearly the same protracted time-span of *ca.* >80 kyr as the interior ages. This suggests that co-erupted crystals record different pre-eruptive thermal histories: some crystals appear to have been isolated from the melt until very briefly before the eruption, whereas others may have crystallized more continuously upon cooling and differentiation of the last major rejuvenation of the magma system. Zircon entrapment and shielding by phenocrysts is a likely scenario for a crystal-rich storage zone (e.g. Bachmann and Bergantz, 2003) that may also be suggested by monazite crystals often hosting fluid inclusions (Fig. 8b), implying crystallization under relatively high volatile content environments. Monazite in volcanic rocks may bear the potential to yield time and geochemical information from a distinct thermochemical window than that offered by zircon in magmatic systems.

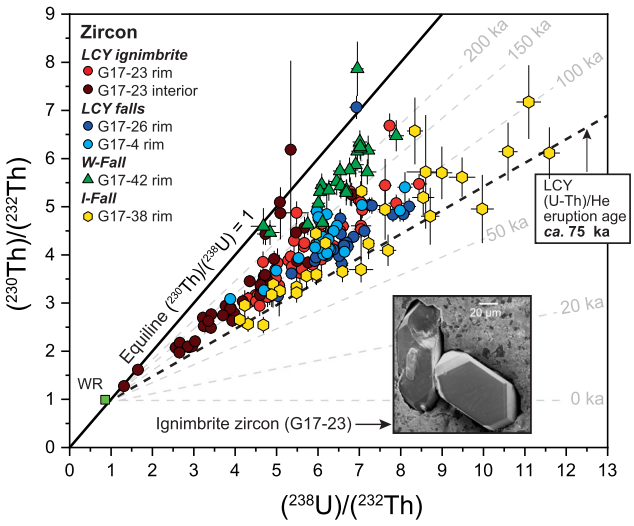


**Figure 9.** $(^{230}Th)/(^{232}Th)$ vs $(^{238}U)/(^{232}Th)$ sphenochron diagram for LCY ignimbrite and falls, W- and I-Fall zircons. U–Th whole-rock isotope composition from Rose and Bornhorst (1981). Equiline defines a secular equilibrium and the upper boundary of the U-series dating method (*ca.* 380 ka). [Color figure can be viewed at wileyonlinelibrary.com]

## *Distribution of PDCs and revised eruptive volume*

Based on field relationships and glass chemical correlations, an updated distribution of PDC deposits for LCY is presented. This includes locations in south-eastern Mexico as the westernmost deposits of LCY ignimbrite ever described, and in the eastern parts of Guatemala, at ≥130 km distance from the source (in a straight line; Fig. 1c). Large-volume PDCs such as those generated by the LCY eruption can overcome large topographic barriers (Aramaki and Ui, 1966; Miller and Smith, 1977; Wilson *et al.*, 1995; Pedrazzi *et al.*, 2019) and reach long-runout distances (Sheridan, 1979; Fisher *et al.*, 1993; Wilson *et al.*, 1995; Bursik and Woods, 1996; Cas *et al.*, 2011; Henry *et al.*, 2012; Roche *et al.*, 2016; Lerner *et al.*, 2019; Shimizu *et al.*, 2019). The evidence for LCY PDCs surmounting several topographic barriers of >400 m elevation difference and subsequently filling valleys over distances

**Table 1.** Summary of zircon (U–Th)/He (ZDD) eruption ages and zircon $^{238}U$–$^{230}Th$ crystallization ages

| Unit | Sample | U–Th dated domain | Literature age (ka) | Zircon (U–Th)/He eruption age (ka) | Zircon $^{238}U$–$^{230}Th$ youngest age (ka) | Bayesian eruption age estimate (ka) |
|---|---|---|---|---|---|---|
| I-Fall | G17-38 | Rims | >40 (Stratigraphy)* | n.d. | $56\ ^{+8}/_{-8}$ | $67\ ^{+11}/_{-9}$ |
| LCY | G17-26 | Rims | 84 ± 5 (O-isotope)† | 75 ± 3 | $74\ ^{+7}/_{-7}$ | $80\ ^{+5}/_{-4}$ |
| | G17-4 | Rims | 84 ± 5 (O-isotope)† | 76 ± 3 | $82\ ^{+10}/_{-9}$ | $85\ ^{+7}/_{-7}$ |
| | G17-23 | Rims | 84 ± 5 (O-isotope)† | 73 ± 4 | $79\ ^{+13}/_{-12}$ | $90\ ^{+5}/_{-5}$ |
| | G17-23 | Interior | 84 ± 5 (O-isotope)† | 73 ± 4 | $81\ ^{+12}/_{-11}$ | $87\ ^{+7}/_{-7}$ |
| "/> | ***Best estimate for LCY eruption age*** | | | **75 ± 2** | **(1σ; *n* = 48; MSWD = 3.3)** | |
| W-Fall | G17-42 | Rims | 158 ± 3 ($^{40}Ar/^{39}Ar$)* | n.d. | $130\ ^{+16}/_{-14}$ | $155\ ^{+24}/_{-19}$ |

Bayesian eruption age estimates are calculated from zircon U–Th age populations following the approach of Keller *et al.* (2018).
*Rose *et al.* (1999).
†Drexler *et al.* (1980).
Best estimate for LCY eruption age was calculated as the weighted mean from all LCY (U–Th)/He individual zircon dates.

>130 km is remarkable. The presence of voluminous distal ignimbrite deposits along the Motagua and Polochic valleys (which represent the tectonic boundaries between the North American and Caribbean plates; Fig. 1c) and in all channels and minor drainages along this regional morphological feature suggests high mobility of the PDCs. However, PDC deposits occurring in isolated basins surrounded by highlands (Koch and Mclean, 1975) could also be explained by currents so voluminous that they radially flooded the entire landscape. The occurrence of abundant charcoal in the distal lapilli-tuff deposits in Chiapas (Mexico), which still reach ~5–10 m in thickness, indicates the preservation of high temperatures to long runout distances.

The LCY ignimbrite volume from a simplistic estimate multiplying area and thickness is ~310 $km^3$ (Fig. 3a). The volume calculated from purely interpolated thicknesses ranges from 286 to 363 $km^3$, with an average of ~320 ± 50 $km^3$ (1 SD; Fig. 3b). Forcing an extrapolation to the estimated 4-m thickness perimeter using synthetic 4-m points reduces the total calculated volume to 258–347 $km^3$, with an average of ~310 ± 40 $km^3$ (1 SD; Fig. 3c). Volumes are heavily influenced by the proximal deposit data. Given the relative sparsity of distal outcrop observations and measured thicknesses, adding synthetic points to force an extrapolation to encompass known outcrops and the estimated depositional extent reduces the influence of the thicker proximal data points in most interpolation algorithms, and reduces the calculated volume by ~3.5% on average. Interpolated thicknesses, however, are based on minimum outcrop thicknesses from often at least partially obscured outcrops, and conservative estimates of inner Quetzaltenango basin fill. Despite the algorithmic reliance on the higher density and thicker proximal and medial deposit observations, the calculated volume measurements between ~310 and 320 $km^3$ are likely to underestimate the total erupted volume of the LCY PDC deposits because only conservative minimum thickness measurements were used as input. The full extent of distal deposits is unknown, particularly towards the southern coastal plain, where it may extend much further than what we have inferred. The depth of filling of proximal basins other than the Quetzaltenango basin is not captured by existing measurements (e.g. Tecpan-Chimaltenango, Guatemala, Totonicapán, San Marcos), which results in volume underestimations due to missing detailed depth information of the other basins. Even this conservative estimate for the volume of the pyroclastic flow deposits at ~310–320 $km^3$ doubles the previously estimated value (Kutterolf *et al.*, 2016). Further refining of these estimates would require identifying the full extent of the distal deposits and the true thickness for proximal basin-filling deposits, which would probably increase the calculated pyroclastic flow volume. The current calculation of the PDC volume in addition to the previously estimated tephra fall-out volume of ~900 ± 90 $km^3$ (Kutterolf *et al.*, 2016) translates to a total erupted tephra volume of ~1220 ± 150 $km^3$ (~730 $km^3$ DRE; $1.53 \times 10^{15}$ kg), confirming the status of LCY as a supereruption. An unknown fraction of the distal fall-out volume, especially in the ocean, is missing from the PDC deposit volume because it reflects co-ignimbrite fall-out. For simplification, it is here included within the fall-out fraction because co-ignimbrite ash distribution follows similar patterns as Plinian fall-out.

## Conclusions

This study provides the first direct radioisotopic dating of the LCY tephra from Atitlán caldera, an important widespread Quaternary marker horizon covering Central America, Mexico, the Eastern Equatorial Pacific, the Caribbean and the Gulf of Mexico. The LCY supereruption occurred at 75 ± 2 ka as the result of protracted magma incubation in a large reservoir where melts probably remained persistently for several tens of thousands of years before the eruption. The LCY climactic supereruption ultimately distributed voluminous tephra that included long-runout PDCs that reached minimum distances >130 km from the source, despite encountering several topographic barriers. New estimates of its minimum erupted (fall-out and PDC deposits) tephra volume yield ~1220 $km^3$, confirming LCY as the first-ever recognized supereruption in Central America.

Moreover, we also determined maximum emplacement ages for the W-Fall and I-Fall eruptions which proved difficult to date in the past. We obtained $^{238}U$–$^{230}Th$ disequilibrium zircon rim ages as young as $130\ ^{+16}/_{-14}$ and $56\ ^{+8.2}/_{-7.7}$ ka, respectively. The zircon (U–Th)/He and $^{238}U$–$^{230}Th$ disequilibria dating techniques are powerful resources to unravel eruption and crystallization timescales of silicic tephra where other geochronological methods have failed.

## Supporting information

Additional supporting information may be found in the online version of this article at the publisher's web-site.

**Table S1**. U–Th zircon ages from large silicic eruptions of Atitlán caldera.

**Table S2**. Major and trace element concentrations from glass shards of selected Atitlán eruptions.

**Table S3**. The Los Chocoyos (U–Th)/He eruption zircon age and parameters used for disequilibrium correction.

**Table S4**. Thickness measurements from PDC from the Los Chocoyos eruption.

## *Data availability statement*

Data are available in the Supporting Information.

*Acknowledgements.* This research was funded through grants SCH 2521/6-1 and KU2685/7-1 by the German National Science Foundation (DFG). INSIVUMEH is thanked for their support during field expeditions. Alexander Varychev from Heidelberg University is thanked for guidance in SEM imaging. Bjarne Friedrichs is thanked for support in the zircon (U–Th)/He data processing. We also thank two anonymous journal reviewers for constructive criticism. Editor Nicholas Balascio is acknowledged for editorial handling of the manuscript. Open Access funding enabled and organized by Projekt DEAL.

*Abbreviations.* DRE, dense rock equivalent; GIS, geographical information system; LCY, Los Chocoyos; MSWD, mean square weighted deviation; PDC, pyroclastic density current; PDF, probability density function; UTM, Universal Transverse Mercator; VEI, Volcanic Explosivity Index; ZDD, zircon double-dating.

# References

Aramaki S, Ui T. 1966. The Aira and Ata pyroclastic flows and related caldera and depressions in southern Kyushu, Japan. *Bulletin Volcanologique* **29**: 29–47.

Bachmann O, Bergantz GW. 2003. Rejuvenation of the Fish Canyon magma body: a window into the evolution of large-volume silicic magma systems. *Geology* **31**: 789–792.

Bachmann O, Charlier BLA, Lowenstern JB. 2007. Zircon crystallization and recycling in the magma chamber of the rhyolitic Kos Plateau Tuff (Aegean arc). *Geology* **35**: 73–76.

Bacon CR, Lowenstern JB. 2005. Late Pleistocene granodiorite source for recycled zircon and phenocrysts in rhyodacite lava at Crater Lake, Oregon. *Earth and Planetary Science Letters* **233**: 277–293.

Bonis S, Bohnenberger O, Stoiber RE *et al*. 1966. Age of pumice deposits in Guatemala. *Geological Society of America Bulletin* **77**: 211–212.

Bowles FA, Jack RN, Carmichael ISE. 1973. Investigation of deep-sea volcanic ash layers from equatorial Pacific cores. *Geological Society of America Bulletin* **84**: 2371–2388.

Brenna H, Kutterolf S, Mills MJ *et al*. 2019. The sulfur- and halogen-rich super eruption Los Chocoyos and its impacts on climate and environment. *Atmospheric Chemistry and Physics Discussions* **2019**: 1–28.

Brenna H, Kutterolf S, Mills MJ *et al*. 2020. The potential impacts of a sulfur- and halogen-rich supereruption such as Los Chocoyos on the atmosphere and climate. *Atmospheric Chemistry and Physics* **20**: 6521–6539.

Brocard G, Morán-Ical SD. 2014. Phreatic clastic dikes and other degassing structures in Los Chocoyos pumice. *Revistã Guatemalteca de Ciencias de la Tierra* **1**: 55–65.

Bursik MI, Woods AW. 1996. The dynamics and thermodynamics of large ash flows. *Bulletin of Volcanology* **58**: 175–193.

Cadet J, Thisse Y, Pouclet A *et al*. 1982b. Tephra from deep-sea drilling project leg-66-Middle America Trench transect (southern Mexico). *Initial Reports of the Deep Sea Drilling Porject* **66**: 687–698.

Cadet J-P, Pouclet A, Thisse Y *et al*. 1982a. Middle America Neogene explosive volcanism and ash layers: evidence from the Middle America Trench transect, deep sea drilling project leg 67. *Initial Reports of the Deep Sea Drilling Project* **67**: 475–491.

Cas RAF, Wright HMN, Folkes CB *et al*. 2011. The flow dynamics of an extremely large volume pyroclastic flow, the 2.08-Ma Cerro Galán Ignimbrite, NW Argentina, and comparison with other flow types. *Bulletin of Volcanology* **73**: 1583–1609.

Danišík M, Schmitt AK, Stockli DF *et al*. 2017. Application of combined U–Th-disequilibrium/U-Pb and (U–Th)/He zircon dating to tephrochronology. *Quaternary Geochronology* **40**: 23–32.

Drexler JW, Rose WI, Sparks RSJ *et al*. 1980. The Los Chocoyos Ash, Guatemala: a major stratigraphic marker in Middle America and in three ocean basins. *Quaternary Research* **13**: 327–345.

Farley K, Kohn B, Pillans B. 2002. The effects of secular disequilibrium on (U–Th)/He systematics and dating of Quaternary volcanic zircon and apatite. *Earth and Planetary Science Letters* **201**: 117–125.

Fisher RV, Orsi G, Ort M *et al*. 1993. Mobility of a large-volume pyroclastic flow – emplacement of the Campanian ignimbrite, Italy. *Journal of Volcanology and Geothermal Research* **56**: 205–220.

Friedrichs B, Atıcı G, Danišík M *et al*. 2021. Sequence modeling in zircon double-dating of Early Holocene Mt. Erciyes domes (Central Anatolia). *Quaternary Geochronology* **61**: 101–129.

Guenthner WR, Reiners PW, Ketcham RA *et al*. 2013. Helium diffusion in natural zircon: radiation damage, anisotropy, and the interpretation of zircon (U-Th)/He thermochronology. *American Journal of Science* **313**, 145–198.

Hahn GA, Rose WI Jr, Meyers T. 1979. Geochemical correlation of genetically related rhyolitic ash-flow and air-fall ashes, central and western Guatemala and the equatorial Pacific. In *Ash-Flow Tuffs*, Chapin CE, Elston WE (eds). Geological Society of America: Denver.

Henry CD, Hinz NH, Faulds JE *et al*. 2012. Eocene–Early Miocene paleotopography of the Sierra Nevada–Great Basin–Nevadaplano based on widespread ash-flow tuffs and paleovalleys. *Geosphere* **8**: 1–27.

Hodell DA, Anselmetti FS, Ariztegui D *et al*. 2008. An 85-ka record of climate change in lowland Central America. *Quaternary Science Reviews* **27**: 1152–1165.

Keller CB, Schoene B, Samperton KM. 2018. A stochastic sampling approach to zircon eruption age interpretation. *Geochemical Perspectives Letters* **8**: 31–35.

Kennett JP, Huddlestun P. 1972. Late Pleistocene paleoclimatology, foraminiferal biostratigraphy and tephrochronology, western Gulf of Mexico. *Quaternary Research* **2**: 38–69.

Kent AJR, Cooper KM. 2018. How well do zircons record the thermal evolution of magmatic systems? *Geology* **46**: 111–114.

Klemetti EW, Clynne MA. 2014. Localized rejuvenation of a crystal mush recorded in zircon temporal and compositional variation at the Lassen Volcanic Center, northern California. *PLOS ONE* **9**: e113157.

Klemetti EW, Deering CD, Cooper KM *et al*. 2011. Magmatic perturbations in the Okataina Volcanic Complex, New Zealand at thousand-year timescales recorded in single zircon crystals. *Earth and Planetary Science Letters* **305**: 185–194.

Koch AJ, Mclean H. 1975. Pleistocene tephra and ash-flow deposits in the volcanic highlands of Guatemala. *Geological Society of America Bulletin* **86**: 529–541.

Krüger K, Kutterolf S, Hansteen TH. 2015. Halogen release from Plinian eruptions and depletion of stratospheric ozone. In *Volcanism and Global Environmental Change*, Schmidt A, Fristad K, Elkins-Tanton L (eds). Cambridge University Press: Cambridge; 244–259.

Kutterolf S, Freundt A, Peréz W. 2008a. Pacific offshore record of Plinian arc volcanism in Central America: 2. Tephra volumes and erupted masses. *Geochemistry, Geophysics, Geosystems* **9**(2 Suppl): 02.

Kutterolf S, Freundt A, Peréz W *et al*. 2008b. Pacific offshore record of plinian arc volcanism in Central America: 1. Along-arc correlations. *Geochemistry, Geophysics, Geosystems* **9**(2 Suppl): 01.

Kutterolf S, Hansteen TH, Freundt A *et al*. 2015. Bromine and chlorine emissions from Plinian eruptions along the Central American Volcanic Arc: from source to atmosphere. *Earth and Planetary Science Letters* **429**: 234–246.

Kutterolf S, Schindlbeck JC, Anselmetti FS *et al*. 2016. A 400-ka tephrochronological framework for Central America from Lake Petén Itzá (Guatemala) sediments. *Quaternary Science Reviews* **150**: 200–220.

Ledbetter M. 1982. Tephrachronology at Sites 502 and 503. *Initial Reports of the Deep Sea Drilling Project* **68**: 403–408.

Ledbetter MT. 1985. Tephrochronology of marine tephra adjacent to Central America. *Geological Society of America Bulletin* **96**: 77–82.

Ledbetter MT, Sparks RSJ. 1979. Duration of large-magnitude explosive eruptions deduced from graded bedding in deep-sea ash layers. *Geology* **7**: 240–244.

Lerner GA, Cronin SJ, Turner GM *et al*. 2019. Recognizing long-runout pyroclastic flow deposits using paleomagnetism of ash. *Geological Society of America Bulletin* **131**: 1783–1793.

Metzner D, Kutterolf S, Toohey M *et al*. 2014. Radiative forcing and climate impact resulting from $SO_2$ injections based on a 200,000-year record of Plinian eruptions along the Central American Volcanic Arc. *International Journal of Earth Sciences* **103**: 2063–2079.

Miller CF, Wark DA. 2008. Supervolcanoes and their explosive supereruptions. *Elements* **4**: 11–15.

Miller TP, Smith RL. 1977. Spectacular mobility of ash flows around Aniakchak and Fisher calderas, Alaska. *Geology* **5**: 173–176.

NASA/METI/AIST/Japan Spacesystems, and U.S./Japan ASTER Science Team. 2019. *ASTER Global Digital Elevation Model V003 [Data set]. NASA EOSDIS Land Processes DAAC*. Accessed 13 June 2019. https://doi.org/10.5067/ASTER/ASTGTM.003

Newhall C, Self S, Robock A. 2018. Anticipating future Volcanic Explosivity Index (VEI) 7 eruptions and their chilling impacts. *Geosphere* **14**: 572–603.

Newhall CG. 1987. Geology of the Lake Atitlan region, western Guatemala. *Journal of Volcanology and Geothermal Research* **33**: 23–55.

Pedrazzi D, Sunye-Puchol I, Aguirre-Díaz G *et al*. 2019. The Ilopango Tierra Blanca Joven (TBJ) eruption, El Salvador: volcano-stratigraphy and physical characterization of the major Holocene event of Central America. *Journal of Volcanology and Geothermal Research* **377**: 81–102.

Pouclet A, Cadet J, Fujioka K *et al*. 1985. Ash layers from Deep-Sea Drilling Project Leg-84 Middle America Trench Transect. *Initial Reports of the Deep Sea Drilling Project* **84**: 609–618.

Rabek K, Ledbetter MT, Williams DF. 1985. Tephrochronology of the western Gulf of Mexico for the last 185,000 years. *Quaternary Research* **23**: 403–416.

Reid MR. 2008. How long does it take to supersize an eruption? *Elements* **4**: 23–28.

Reiners PW. 2005. Zircon (U-Th)/He thermochronometry. *Reviews in Mineralogy and Geochemistry* **58**: 151–179.

Reiners PW, Spell TL, Nicolescu S *et al*. 2004. Zircon (U-Th)/He thermochronometry: He diffusion and comparisons with $^{40}Ar/^{39}Ar$ dating. *Geochimica et Cosmochimica Acta* **68**: 1857–1887.

Rivera TA, Schmitz MD, Jicha BR *et al*. 2016. Zircon petrochronology and $^{40}Ar/^{39}Ar$ sanidine dates for the Mesa Falls Tuff: crystal-scale records of magmatic evolution and the short lifespan of a large Yellowstone magma chamber. *Journal of Petrology* **57**: 1677–1704.

Roche O, Buesch DC, Valentine GA. 2016. Slow-moving and far-travelled dense pyroclastic flows during the Peach Spring super-eruption. *Nature Communications* **7** 10890.

Rose WI, Bornhorst TJ. 1981. *Uranium and Thorium in Selected Quaternary Volcanic Rocks of Guatemala and Sumatra: Evidence for Uranium Redistribution*. American Association of Petroleum Geologists: Tulsa.

Rose WI, Conway FM, Pullinger CR *et al*. 1999. An improved age framework for late Quaternary silicic eruptions in northern Central America. *Bulletin of Volcanology* **61**: 106–120.

Rose WI, Grant NK, Easter J. 1979. Geochemistry of the Los Chocoyos Ash, Quezaltenango Valley, Guatemala. *Geological Society of America Special Papers* **180**: 87–100.

Rose WI, Newhall CG, Bornhorst TJ *et al*. 1987. Quaternary silicic pyroclastic deposits of Atitlán Caldera, Guatemala. *Journal of Volcanology and Geothermal Research* **33**: 57–80.

Schindlbeck JC, Kutterolf S, Freundt A *et al*. 2018. Miocene to Holocene marine tephrostratigraphy offshore northern Central America and southern Mexico: pulsed activity of known volcanic complexes. *Geochemistry, Geophysics, Geosystems* **19**: 4143–4173.

Schmitt AK. 2011. Uranium series accessory crystal dating of magmatic processes. *Annual Review of Earth and Planetary Sciences* **39**: 321–349.

Schmitz MD, Bowring SA. 2001. U–Pb zircon and titanite systematics of the Fish Canyon Tuff: an assessment of high-precision U–Pb geochronology and its application to young volcanic rocks. *Geochimica et Cosmochimica Acta* **65**: 2571–2587.

Self S. 2006. The effects and consequences of very large explosive volcanic eruptions. *Philosophical Transactions. Series A, Mathematical, Physical, and Engineering Sciences* **364**: 2073–2097.

Sheridan MF. 1979. Emplacement of pyroclastic flows: a review. *Geological Society of America Special Papers* **180**: 125–136.

Shimizu HA, Koyaguchi T, Suzuki YJ. 2019. The run-out distance of large-scale pyroclastic density currents: A two-layer depth-averaged model. *Journal of Volcanology and Geothermal Research* **381**: 168–184.

Simon JI, Renne PR, Mundil R. 2008. Implications of pre-eruptive magmatic histories of zircons for U–Pb geochronology of silicic extrusions. *Earth and Planetary Science Letters* **266**: 182–194.

Vermeesch P. 2018. IsoplotR: A free and open toolbox for geochronology. *Geoscience Frontiers* **9**: 1479–1493.

Wilson CJN, Houghton BF, Kampt PJJ *et al*. 1995. An exceptionally widespread ignimbrite with implications for pyroclastic flow emplacement. *Nature* **378**: 605–607.

Wotzlaw J-F, Bindeman IN, Watts KE *et al*. 2014. Linking rapid magma reservoir assembly and eruption trigger mechanisms at evolved Yellowstone-type supervolcanoes. *Geology* **42**: 807–810.